Warm-Route versus Cold-Route Interbasin Exchange in the Meridional Overturning Circulation

PAOLA CESSI AND C. S. JONES

Scripps Institution of Oceanography, University of California, San Diego, La Jolla, California

(Manuscript received 8 November 2016, in final form 2 June 2017)

ABSTRACT

The interbasin exchange of the meridional overturning circulation (MOC) is studied in an idealized domain with two basins connected by a circumpolar channel in the southernmost region. Gnanadesikan's conceptual model for the upper branch of the MOC is extended to include two basins of different widths connected by a reentrant channel at the southern edge and separated by two continents of different meridional extents. Its analysis illustrates the basic processes of interbasin flow exchange either through the connection at the southern tip of the long continent (cold route) or through the connection at the southern tip of the short continent (warm route). A cold-route exchange occurs when the short continent is poleward of the latitude separating the subpolar and subtropical gyre in the Southern Hemisphere (the zero Ekman pumping line); otherwise, there is warm-route exchange. The predictions of the conceptual model are compared to primitive equation computations in a domain with the same idealized geometry forced by wind stress, surface temperature relaxation, and surface salinity flux. Visualizations of the horizontal structure of the upper branch of the MOC illustrate the cold and warm routes of interbasin exchange flows. Diagnostics of the primitive equation computations show that the warm-route exchange flow is responsible for a substantial salinification of the basin where sinking occurs. This salinification is larger when the interbasin exchange is via the warm route, and it is more pronounced when the warm-route exchange flows from the wide to the narrow basin.

1. Introduction

The higher North Atlantic sea surface salinity promotes regular deep convection events that are prevented in the North Pacific by a strong halocline (Warren 1983). The salinification of the North Atlantic occurs partly by transport of high-salinity water from the subtropics that replenishes the surface water masses that are removed by convection. This haline densification overcomes the buoyancy increase by warming associated with the northward transport of waters (Warren 1983; Broecker 1991). The net result is a positive salt feedback that favors deep-water mass formation and the maintenance of the meridional overturning circulation (MOC; Stommel 1961).

In order for convection to reach deep levels, there must be deep fluid that is more buoyant than fluid at the surface. Because there is no deep source of buoyant fluid,[1] mechanical processes must push buoyant fluid down from the surface, generating deep stratification. In addition, the mechanically convected water masses must return to the ocean surface, that is, they must be upwelled somewhere. Thus, deep stratification and upwelling are determined by two processes: 1) deep-reaching, wind-driven Ekman suction in the circumpolar portion of the Southern Ocean (Toggweiler and Samuels 1993) and 2) diapycnal mixing due to breaking internal gravity waves (Munk 1966). The latter process operates in all oceans and is most effective in the surface mixed layer and below approximately 2000 m, where rough topography enhances the turbulent direct cascade (St. Laurent et al. 2002; Nikurashin and Ferrari 2013). The net result is that the MOC is a global circulation primarily linking processes in the high latitudes of the North Atlantic (deep convection) and the high latitudes of the Southern Ocean (Ekman suction and deep stratification generation), with secondary contributions from the Indian and Pacific Oceans (diapycnal mixing).

Given that the MOC is a global process, an obvious question is what makes the North Atlantic the preferred

[1] We neglect the buoyancy flux from geothermal heating because it does not influence the ocean above the abyss.

Corresponding author: Paola Cessi, pcessi@ucsd.edu

DOI: 10.1175/JPO-D-16-0249.1

location for deep-water formation, and why is the salt feedback not operative in the North Pacific? Transient North Pacific deep-water formation, with an interhemispheric meridional cell in the Pacific, likely occurred during the Last Glacial Termination (Okazaki et al. 2010), but the Pacific meridional overturning circulation (PMOC) lasted less than 3000 yr. Both idealized (Hughes and Weaver 1994; Jones and Cessi 2016) and comprehensive ocean models (Zhang and Delworth 2005) show that a substantial freshwater perturbation is needed to weaken the Atlantic MOC (AMOC).

Several reasons for preferring the AMOC over the PMOC have been put forward [see Weaver et al. (1999) for a review], some extrinsic to the ocean (e.g., orographically enhanced precipitation in the Indo-Pacific sector) and others intrinsic to the ocean circulation. In the latter category, which is the focus of this work, two geometrical characteristics favor the Atlantic: its narrower width and the difference between the southward extent of the American and African continents (Reid 1961; Gordon 1986; Nilsson et al. 2013).

The narrower width of the North Atlantic implies that the southward western boundary velocity due to the locally wind-driven subpolar gyre is weaker than that in the North Pacific (assuming that the wind stress at these latitudes is approximately the same over both sectors), while the northward western boundary velocity associated with the MOC is approximately the same. These two contributions to the western boundary current in the subpolar region result in a stronger northward flow at the western boundary of the narrower basin, enabling the northward transport of salinity from the subtropical region. Therefore, the salt advection feedback is more effective in a narrow basin. This mechanism relies on the assumption that the wind stress and the MOC transport are approximately the same over the two basins. As shown in Jones and Cessi (2016), the rate of sinking is determined by the rate of upwelling: the Ekman upwelling in the circumpolar region of the Southern Ocean and the global diapycnal mixing. Therefore, the MOC transport is approximately independent of the sinking location for fixed wind stress and diapycnal mixing.

The low-latitude extent of the tip of South Africa relative to South America has been invoked as a favorable configuration for transporting high-salinity subtropical water from the Indo-Pacific sector into the Atlantic (Reid 1961; Gordon 1986). In particular, this hypothesis relies on the assumption that a larger fraction of the MOC upper branch returns from the Indo-Pacific to the Atlantic around the tip of Africa (the warm route) rather than around the tip of South America (the cold route; Rintoul 1991; Gordon et al. 1992), as depicted in Fig. 1. Lagrangian analyses of coarse-resolution ocean models confirm that in the present climate the upper branch of the MOC returns waters upwelled in the Indo-Pacific sector to the Atlantic preferentially through the warm route (Speich et al. 2001), enhancing the salt feedback. Some authors have identified the northern, westward branch of the Southern Ocean subtropical "supergyre" as an essential element of the warm route (Nilsson et al. 2013), while others have emphasized the southern, eastward component of the supergyre (Durgadoo et al. 2013). Here, we present arguments indicating that all of the supergyre enables the warm-route exchange of the MOC. Specifically, we show that the position of the short continent relative to the latitude of the zero Ekman pumping determines whether the cold route or the warm route is the preferred mode of interbasin exchange. We find that as long as there is a subtropical supergyre connecting the South Atlantic to the Indo-Pacific, the exchange is via the warm route. Conversely, if the subtropical gyres in the Atlantic and Indo-Pacific sectors are separated, then the interbasin flow is via the cold route.

In this study, we examine the conditions required for the warm-route versus the cold-route in the connection between the Indo-Pacific and the Atlantic. Our approach is to consider two models: 1) an ocean-only general circulation model, obeying the three-dimensional primitive equation, with simplified geometry and forcing; and 2) a modification of Gnanadesikan's (1999) conceptual model for the residual buoyancy budget of the upper branch of the MOC, which includes two basins with a circumpolar connection to the south. The conceptual model cannot predict where sinking occurs, but, once the sinking location is prescribed, it makes predictions about key quantities, such as the amount of sinking and the strength of the interbasin transport. The spirit of this work is very similar to that of Ferreira et al. (2010) and Nilsson et al. (2013), except that the ocean-only configuration enables examination of the ocean response to different geometries under prescribed wind and buoyancy forcing; confounding effects of atmospheric feedbacks are eliminated. In particular, we focus on the latitude of the short continent separating the active, sinking basin (the model Atlantic) from the passive, nonsinking basin (the model Indo-Pacific), keeping the wind stress and buoyancy forcing fixed.

Because of our focus on salt transport, it is more useful to think about the residual overturning circulation (ROC) rather than the Eulerian MOC; the ROC is more indicative than the MOC of the tracer transport. Thus, both our conceptual model and the diagnostics of the GCM are in terms of the ROC.

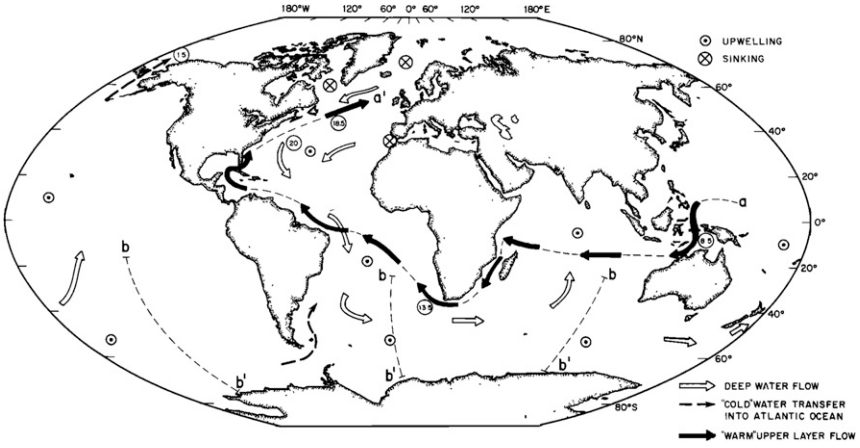

FIG. 1. Structure of the global MOC according to Fig. 2a of Gordon (1986, reproduced here). The thick black arrows represent the warm-water route, while the dashed arrow is the cold-water route. Both routes are flows of upper-layer water returning the deep-water flow depicted in white large arrows.

2. A conceptual model of the upper branch of the ROC

The essential ingredients for interbasin transport in the upper branch of the ROC are summarized in an extension of the model by Gnanadesikan (1999) to two basins connected by a circumpolar region (Allison 2009; Jones and Cessi 2016). As in Gnanadesikan (1999), the conceptual model considers the residual buoyancy budget vertically integrated from the surface down to an isopycnal $b = b_m$, whose time-averaged depth h depends on position. The buoyancy surface b_m divides the upper and lower branches of the ROC and outcrops both in the circumpolar region and in the Northern Hemisphere of the sinking basin. A schematic of the geometry of the domain, of the isopycnal b_m, and of the processes participating in the residual budget is shown in Fig. 2. The geography is simplified: we consider two basins of different widths, bounded by thin continents of different lengths, oriented along meridians. The two basins are connected at the southern end by a circumpolar region. A plan view of the geometry and notation of the model is shown in Fig. 3. Using the constraints of mass

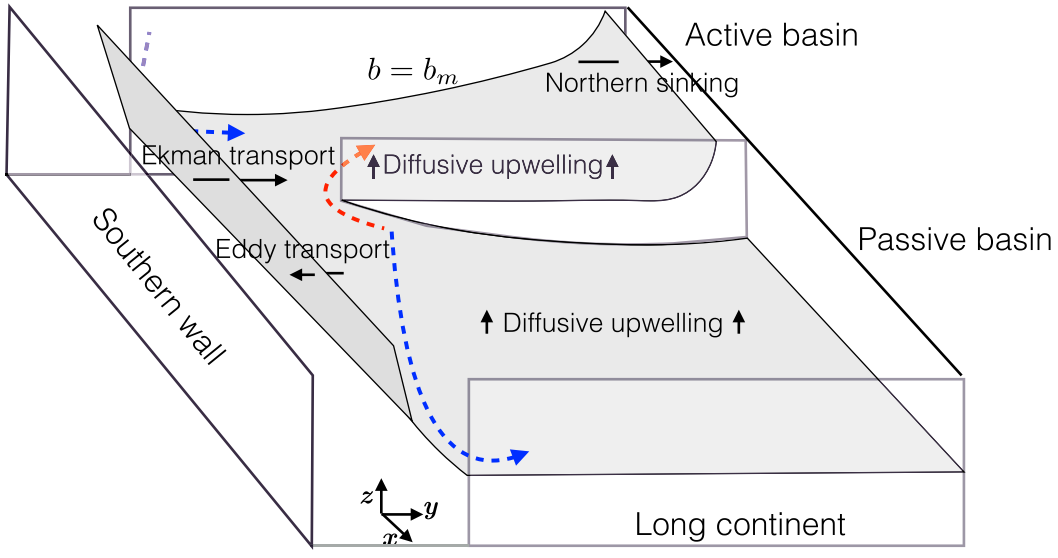

FIG. 2. Geometry of the conceptual model: the budget for the residual circulation above the isopycnal dividing the upper and lower branch of the MOC is examined. The dashed red and blue lines indicate the warm- and cold-route exchanges, respectively.

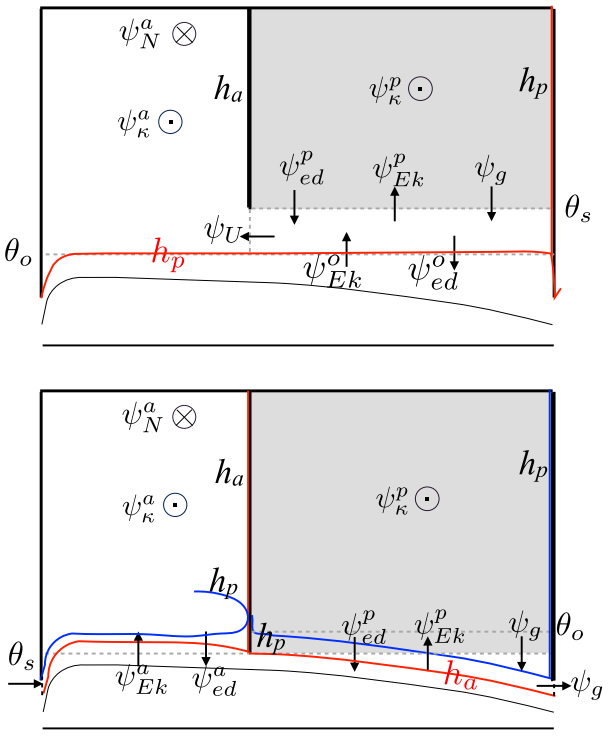

FIG. 3. Schematic of the two-basin box model, showing the residual buoyancy budget above the isopycnal b_m, bounding the upper branch of the ROC. Sinking is in the basin with the short continent to the east (the a basin), and it is denoted by $\otimes$, while upwelling is denoted by $\odot$. The ψ_N denotes northern sinking, ψ_κ denotes diffusive upwelling, $\psi_{\rm Ek}$ denotes the Ekman transport, $\psi_{\rm ed}$ denotes the transport due to eddies, ψ_g denotes a geostrophically balanced transport, and ψ_U denotes the warm-route interbasin transfer. The thick solid lines represent the boundaries (continents), and the thin lines are contours of constant depth of the isopycnal b_m; h_a is the height at the eastern boundary of the active (sinking) basin, and h_p is the height at the eastern boundary of the passive (nonsinking) basin. The gray, dashed lines are lines of constant latitude or longitude. The red line shows the position of the northernmost circumpolar depth of b_m. In the top panel, the equatorward boundary of the Southern Hemisphere subpolar gyre, that is, the zero Ekman pumping line at latitude θ_o, is south of the short continent, which terminates at latitude θ_s. In this case, the northern boundary of the circumpolar flow approximately coincides with the isopycnal depth h_p, and it is not possible to have a cold-route interbasin exchange flow. In the bottom panel, θ_o is north of θ_s and the interbasin flow occurs on the southern edge of the long continent. The arrows point in the direction of the sense of circulation, but in the budget equations the eastward, northward, and upward transports are counted positive. The superscripts "a" and "p" refer to the active and passive basin, respectively.

conservation (in buoyancy coordinates) and geostrophy together with simple assumptions about the form of the ageostrophic transports (Ekman flow, diapycnal upwelling, and eddy fluxes), the box model makes predictions on a few key quantities, such as the height of the isopycnal b_m, h, and the different components of the buoyancy transport ψ at key locations. In particular, the components of ψ can be related to the heights of the isopycnal b_m at the eastern boundaries of the basins h_a and h_p in Fig. 3, which, by geostrophy and the no-normal flow condition, are constant.

The main assumption in the formulation is that all sinking occurs at the northern end of the basin with the short continent to the east (this is called the active basin), excluding the possibility that part of the sinking might occur in the basin with the long continent to the east (called the passive basin). This assumption is supported by the idealized modeling studies of Ferreira et al. (2010) and Nilsson et al. (2013).

With reference to Fig. 3, we must consider two different situations, depending on whether the boundary between the Southern Hemisphere subpolar and subtropical gyres at latitude θ_o (also known as the zero Ekman pumping line) is poleward or equatorward of the short-continent southern tip, located at latitude θ_s. We assume that in all cases, the tip of the long continent is poleward of θ_o, that is, in the Ekman upwelling region.

If $|\theta_s| < |\theta_o|$, the buoyancy surface b_m has an uninterrupted isocontour of constant depth h_o, connecting circumpolarly the end point of the long continent, across which no vertically integrated meridional geostrophic flow can occur (this is the red contour in the top panel of Fig. 3); this contour marks the southern boundary of the Southern Ocean subtropical gyre and the northern boundary of the circumpolar circulation that replaces the subpolar gyre in the Southern Hemisphere. Because this depth contour grazes the eastern boundary of the passive basin, we have $h_o \approx h_p$, where h_p is the constant depth of the target buoyancy on the eastern boundary of the passive basin; the approximation involves neglecting the effects of the eddy transport of buoyancy, although they are not completely negligible at the end of the long continent (Gill 1968; Marshall et al. 2016). In this case, there cannot be a cold-route exchange between the two basins. Because there cannot be any net geostrophic flow across this circumpolar contour, the maximum northward Ekman transport across the depth contour $h_o \approx h_p$ proceeds north to feed the upper branch of the ROC. The portion of the Ekman transport that enters the passive basin sector makes its way to the active basin via the warm route, as shown by the red dashed line in Fig. 2, through the flow marked ψ_U in the top panel of Fig. 3. In practice, in the box model calculation that follows, we approximate the components of the transport across this northernmost circumpolar contour with their values at the line of constant latitude $\theta = \theta_o$, indicated by the long, horizontal, dashed line in the top panel of Fig. 3.

If $|\theta_s| > |\theta_o|$, the northernmost circumpolar isocontour for the depth of the buoyancy surface b_m is h_a, that is, the depth at the eastern boundary of the short continent (the

red line in the bottom panel of Fig. 3). Conversely, the isocontour of value h_p intercepts the short continent (blue line in the bottom panel of Fig. 3). Thus, there is a pressure difference between the isocontours h_a and h_p at the end of the long continent; in this case, the interbasin exchange occurs via the cold route through the term ψ_g. The average latitude of the northernmost circumpolar contour is θ_s, and the Ekman transport entering the basins from the circumpolar region is lower than the maximum value. This case has already been considered by Jones and Cessi (2016) in the special case of equal continents' lengths, and there are no qualitative differences when the continents' lengths differ.

The factor determining the cold- or warm-route regime is the position of the boundary dividing the Southern Hemisphere subtropical and subpolar gyre: For the warm-route case, this latitude is south of the short-continent tip, and there is a single subtropical gyre connecting the two basins, which allows the Ekman transport entering the passive basin to exit it along the western boundary of the short continent. For the cold-route case, the short-continent tip penetrates into the subpolar, circumpolar region of the Southern Hemisphere, and the interbasin flow occurs in an eastward zonal flow at the tip of the long continent.

With reference to the top panel of Fig. 3, we consider the residual buoyancy budget above b_m for two regions: the passive basin north of θ_s (the gray region in the top panel of Fig. 3) and the whole region north of the isoline h_p at latitude θ_o. The eastward, northward, and upward transports are counted positive, but the arrows in Fig. 3 point in the direction of the flow. If θ_s is equatorward of θ_o, we have

$$\psi^p_{\rm Ek} + \psi^p_{\rm ed} + \psi^p_\kappa + \psi_g = 0, \quad \text{and} \tag{1}$$

$$\psi^o_{\rm Ek} + \psi^o_{\rm ed} + \psi^a_\kappa + \psi^p_\kappa = \psi^a_N, \tag{2}$$

where ψ_κ denotes diffusive upwelling, ψ_g denotes geostrophically balanced transport, ψ_N denotes northern sinking, and $\psi^o_{\rm Ek}$ and $\psi^o_{\rm ed}$ are the Ekman and eddy transports across the northernmost circumpolar depth contour, respectively. We can also calculate the warm-route transport using the mass budget in the region between θ_s and θ_o in the passive basin sector. This budget gives

$$\psi_U = -r\psi^o_{\rm Ek} - r\psi^o_{\rm ed} + \psi^p_{\rm Ek} + \psi^p_{\rm ed} + \psi_g, \tag{3}$$

where $r \equiv L_p(\theta_o)/L(\theta_o)$ is the ratio of the width of the passive basin L_p to the width of the circumpolar region L at θ_o. The important point here is that the Ekman transport (minus the eddy flux of buoyancy plus the diapycnal transport) entering the passive basin sector from the circumpolar region must be diverted toward the active basin in a net westward flow via the warm route. In contrast, in the arrangement shown in the bottom panel of Fig. 3, the passive basin portion of the circumpolar Ekman transport (minus the eddy flux of buoyancy plus the diapycnal transport) flows eastward along the circumpolar current before being diverted along the western boundary of the active basin via the cold route, through the term ψ_g.

The main unknowns in (1) and (2) are the depths h_a and h_p (we assume that $h_o = h_p$, even though this is not completely accurate when eddy fluxes are present). We must thus relate all the transports terms to the two unknowns h_a and h_p, and this is not obvious for the eddy and diapycnal terms. To compare with previous work, we use the same relations used by previous authors (Gnanadesikan 1999; Allison 2009; Jones and Cessi 2016) so that (1) and (2) become

$$\underbrace{-\frac{\tau_s L_p(\theta_s)}{\rho_0 f_s}}_{\psi^p_{\rm Ek}} \underbrace{-\frac{\kappa_{\rm GM} h_p L_p(\theta_s)}{L_s}}_{\psi^p_{\rm ed}} + \underbrace{\frac{\kappa A_p}{h_p}}_{\psi^p_\kappa} + \underbrace{\frac{g'(h_p^2 - h_a^2)}{2f_s}}_{\psi_g} = 0,$$

and

(4)

$$\underbrace{-\frac{\tau_o L(\theta_o)}{\rho_0 f_o}}_{\psi^o_{\rm Ek}} \underbrace{-\frac{\kappa_{\rm GM} h_p L(\theta_o)}{L_o}}_{\psi^o_{\rm ed}} + \underbrace{\frac{\kappa A_a}{h_a}}_{\psi^a_\kappa} + \underbrace{\frac{\kappa A_p}{h_p}}_{\psi^p_\kappa} = \underbrace{g'\frac{h_a^2}{2f_n}}_{\psi^a_N}.$$

(5)

The wind stress at $\theta_{s,o}$ is $\tau_{s,o}$, $f_{s,o}$ is the Coriolis parameter at the same two latitudes, f_n is the Coriolis parameter at the sinking latitude, $\kappa_{\rm GM}$ is the coefficient of Gent–McWilliams eddy fluxes parameterization, κ is the interior diapycnal diffusivity, $A_{a,p}$ are the areas of the semienclosed basins, $L_{s,o}$ is the meridional distance between $\theta_{s,o}$ and the southern edge of the channel, and g' is the range of surface buoyancies shared by the sinking and circumpolar regions. The values of the prescribed parameters are given in Table 1. With reference to the top panel of Fig. 3, the interbasin exchange ψ_U can be obtained from the residual budget (3), using (4), and it is given by

$$\psi_U = \frac{\tau_o L_p(\theta_o)}{\rho_0 f_o} + \frac{\kappa_{\rm GM} h_p L_p(\theta_o)}{L_o} - \frac{\kappa A_p}{h_p}. \tag{6}$$

The exchange flow is in geostrophic balance and thus $hu = -g'/(2f)\partial_y h^2$. Because of the full variation of the Coriolis parameter with latitude, it is not possible to express $\psi_U \equiv \int_{R\sin\theta_o}^{R\sin\theta_s} hu\, dy$ solely in terms of the heights h_a and h_p (R is the radius of the spherical domain).

If θ_s is poleward of θ_o, (4) remains unchanged, but (5) is replaced by the budget in the active sector north of the

TABLE 1. The external parameters for the simplified two-basin transport budget, as deduced from the numerical simulations.

Parameter	Value	Notes
κ_{GM}	$500\,m^2\,s^{-1}$	Value used in the numerical model.
L_p	10 000 km	Width of the wide basin at −52.5°.
L_a	5000 km	Width of the narrow basin at −52.5°.
L_c	2000 km	North–south extent of the channel.
A_a	$5(\sin\lvert\theta_s\rvert + 1) \times 10^{13}\,m^2$	Area of the narrow basin north of θ_s.
A_p	$10(\sin\lvert\theta_s\rvert + 1) \times 10^{13}\,m^2$	Area of the wide basin north of θ_s.
ρ_0	$1000\,kg\,m^{-3}$	The average density.
f_n	$1.2 \times 10^{-4}\,s^{-1}$	f at 52.5°.
κ	$2 \times 10^{-5}\,m^2\,s^{-1}$	Value used in the numerical model.
τ_o	0.1 Pa	Maximum wind stress at $\theta = \theta_o$.
g'	$0.004\,m\,s^{-2}$	Approximate range of buoyancy shared between the channel and the northern end of the active basin.

isocontour h_a, whose average latitude is approximately $\theta = \theta_s$ (cf. the bottom panel of Fig. 3), and it is given by

$$\underbrace{-\frac{\tau_s L_a(\theta_s)}{\rho_0 f_s}}_{\psi^a_{\mathrm{Ek}}} \underbrace{-\frac{\kappa_{\mathrm{GM}} h_a L_a(\theta_s)}{L_s}}_{\psi^a_{\mathrm{ed}}} + \underbrace{\frac{\kappa A_a}{h_a}}_{\psi^a_{\kappa}} \underbrace{-\frac{g'(h_p^2 - h_a^2)}{2f_s}}_{\psi_g} = \underbrace{g'\frac{h_a^2}{2f_n}}_{\psi^a_N}. \tag{7}$$

The geostrophic transport ψ_g is then proportional to the difference between the squared depths of the isopycnal b_m at the eastern boundaries of each basin (Jones and Cessi 2016).

There are two assumptions made in (4), (5), and (7): 1) the geostrophic transport is independent of depth within the upper branch of the ROC, and 2) at the southern edge of the continents the depth of the isopycnals has the same value along both sides of the continent, that is, the normal flow into the southern edge of the continent is balanced geostrophically.

When θ_s is north of θ_o, the system (4) and (5) is solved for $h_{a,p}$, given the external parameters for geometry, forcing, and diffusion. When θ_s is south of θ_o, the system (4) and (7) is solved instead. Solutions for $h_{a,p}$ and $\psi_{N,U}$ are presented in Fig. 4.[2] The essential point is that for $|\theta_s| < |\theta_o|$ the ROC is approximately independent of θ_s and approximately given by the maximum Ekman transport in the Southern Ocean region. For most values

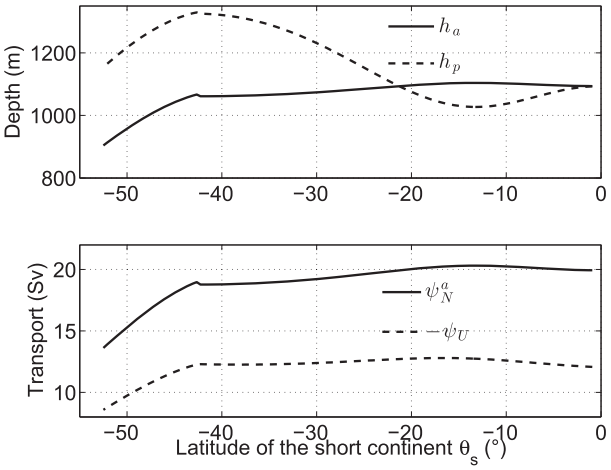

FIG. 4. (top) The solutions h_a (solid) and h_p (dashed) of (5) and (4) and (bottom) the associated sinking ψ^a_N (solid) and minus the interbasin exchange $-\psi_U$ (dashed), as a function of the short-continent latitude θ_s. Parameters are fixed to the values of Table 1: the maximum Ekman transport (17.5 Sv) occurs at $\theta_o = -43°$. For $|\theta_s| < |\theta_o|$ it is not possible to have a cold-route interbasin exchange flow, while for $|\theta_s| > |\theta_o|$ the warm route is not possible; instead the interbasin flow occurs around the southern edge of the long continent, and we set $\psi_U = \psi_g$, even though in this case the zonal flow is positive.

of θ_s the passive basin is deeper than the active one, a result already discussed in Jones and Cessi (2016). In the region of equatorial easterlies $h_p < h_a$, but this does not imply that the interbasin exchange flow changes sign, as might be erroneously inferred by assuming that $\psi_U \sim h_p - h_a$. Instead, ψ_U carries the Ekman transport entering the passive basin, which is approximately independent of θ_s according to the simple conceptual model. We note that in the bottom panel of Fig. 4, we set $\psi_U = \psi_g$ for $\theta_s < \theta_o$ but that the zonal flow around the corner of the long continent is actually eastward, that is, positive, while $\psi_g < 0$.

To understand these properties it is useful to examine the limit where $\kappa = \kappa_{\mathrm{GM}} = 0$. In the nondiffusive limit we have, for $|\theta_s| < |\theta_o|$,

$$h_p^2 = \frac{2}{g'\rho_0}\left[\tau_s L_p(\theta_s) - \tau_o L(\theta_o)\frac{f_n}{f_o}\right], \quad \text{and} \tag{8}$$

$$h_a^2 = -\frac{2f_n \tau_o L(\theta_o)}{g'\rho_0 f_o}, \tag{9}$$

and the warm-route interbasin transport is

$$\psi_U = \frac{\tau_o}{\rho_o f_o} L_p(\theta_o). \tag{10}$$

The total amount of sinking is given by the zonally integrated maximum Ekman transport at the latitude of

[2] The small discontinuity at $\theta_s = \theta_o$ is due to the approximation $h_o \approx h_p$.

zero Ekman pumping, proportional to τ_o. In the same limit, for $|\theta_s| > |\theta_o|$, we have

$$h_p^2 = \frac{2}{g'\rho_0}\tau_s\left[L_p(\theta_s) - L(\theta_s)\frac{f_n}{f_s}\right], \quad \text{and} \tag{11}$$

$$h_a^2 = -\frac{2f_n\tau_s L(\theta_s)}{g'\rho_0 f_s}. \tag{12}$$

In both cases, the limits (8), (9), (11), and (12) clearly show that for τ_s or τ_o positive, $h_p > h_a$, that is, the isopycnal b_m is shallower in the active, sinking basin than in the passive basin. This is because ψ_g needs to be negative in order to return the northward-flowing Ekman transport through a geostrophically balanced flow out of the passive basin.

The simple conceptual model assumes that sinking will occur in one basin. The missing information needed to determine whether there are multiple sinking locations concerns the surface buoyancy field and in particular the extent of the buoyancy values shared between the circumpolar region and the Northern Hemisphere. Crucial to this knowledge is the salinity distribution, determined by advection and diffusion of the salinity subject to the prescribed surface flux. This process is beyond the scope of the simple conceptual model developed here, and instead we turn to a primitive equation general circulation model (GCM), discussed in the following sections.

3. Model and diagnostics

The numerical model employed is the Massachusetts Institute of Technology GCM (MITgcm; Marshall et al. 1997a,b), which integrates the hydrostatic, Boussinesq primitive equations. The domain is a spherical sector spanning 140° in latitude and 210° in longitude with a 1° horizontal resolution. The geometry consists of two idealized basins, one twice as wide as the other, connected at the southern edge of the domain by a periodic channel of minimum latitudinal width 17.5° as shown in Fig. 5. The bottom is flat and 4000 m deep, except for a sill in the periodic channel, one grid point wide, and 1333 m high, located immediately south of the narrow basin's western boundary. There are 32 unequally spaced levels in the vertical, ranging from a minimum spacing of 13.6 m at the top to a maximum of 286 m at the bottom.

The equation of state is linear, so that the buoyancy is described by

$$b = g[\alpha_T T - \beta_S(S - S_{\text{ref}})], \tag{13}$$

where $\alpha_T = 2\times10^{-4}\,^\circ\text{C}^{-1}$, $\beta_S = 7.4\times10^{-4}$, and $S_{\text{ref}} = 35$. Salinity is given on the practical salinity scale, and therefore it is quoted without units.

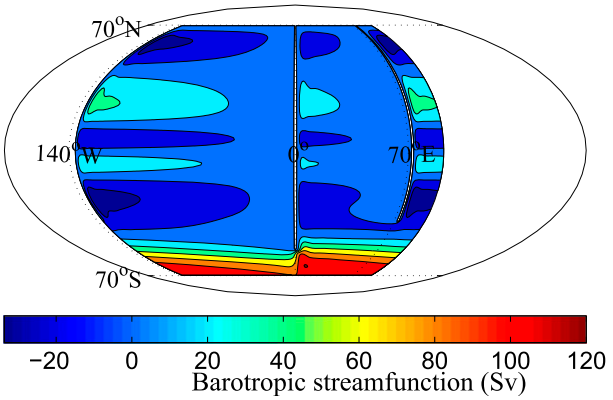

FIG. 5. Barotropic streamfunction and geometry of the domain used in the computations. The length of the continents is varied between simulations; in this figure, the long continent terminates at $\theta = -52.5°$, and the short continent terminates at $\theta = -35°$. The domain is 140° in latitude, 210°-periodic in longitude, and 4000 m deep, and the westernmost 20° of the domain is repeated to the right of the figure.

The surface forcings are steady and zonally uniform; the expressions for the wind stress τ, freshwater flux F, and distribution to which the surface temperature is relaxed T^* are given by

$$\tau = \tau_{\text{Max}}[-\cos(3\pi\theta/140) + e^{-\theta^2/\sigma^2}], \tag{14}$$

$$F = F_{s0}[\cos(7\pi\theta/8\Theta) - 2e^{-(\theta/\Theta)^2/(2\sigma_F^2)}] - F_0, \quad \text{and} \tag{15}$$

$$T^* = T_{\text{eq}}[\cos(\pi\theta/140)^2 + 0.1e^{-(\theta/2\Theta-1)^2}]. \tag{16}$$

We adopt the following notation: θ is latitude in degrees, $\tau_{\text{Max}} = 0.1$ Pa, $\sigma = 10°$, $F_{s0} = 2\times10^{-8}\,\text{m s}^{-1}$, $\sigma_F = 0.128$, $\Theta = 60°$, and $T_{\text{eq}} = 25°$C. The relaxation time scale for the surface temperature is 10 days. The constant F_0 is defined such that the area-averaged freshwater flux $\langle F\rangle = 0$. The freshwater flux is then turned into a virtual salt flux by multiplying F by -35. The distributions of τ, F, and T^* as a function of latitude are shown in Fig. 6.

Momentum is dissipated via Laplacian viscosity with horizontal and vertical coefficients $\nu_h = 4\times10^4\,\text{m}^2\,\text{s}^{-1}$ and $\nu_v = 1\times10^{-4}\,\text{m}^2\,\text{s}^{-1}$, respectively; we employ no-slip sidewalls and a no-slip bottom augmented by a linear bottom drag with coefficient $r = 3.5\times10^{-6}\,\text{s}^{-1}$ applied over the bottom grid cell. Because of the coarse model resolution, baroclinic eddies are parameterized using the advective form of Gent and McWilliams (1990, hereinafter GM) and Redi (1982) isopycnal mixing with equal mixing coefficients $\kappa_{\text{GM}} = 500\,\text{m}^2\,\text{s}^{-1}$. GM is implemented using the boundary value problem scheme of Ferrari et al. (2010) with vertical mode number $m = 2$ and minimum wave speed $c_{\text{min}} = 0.1\,\text{m s}^{-1}$. The Redi tensor is tapered exponentially to horizontal diffusion in

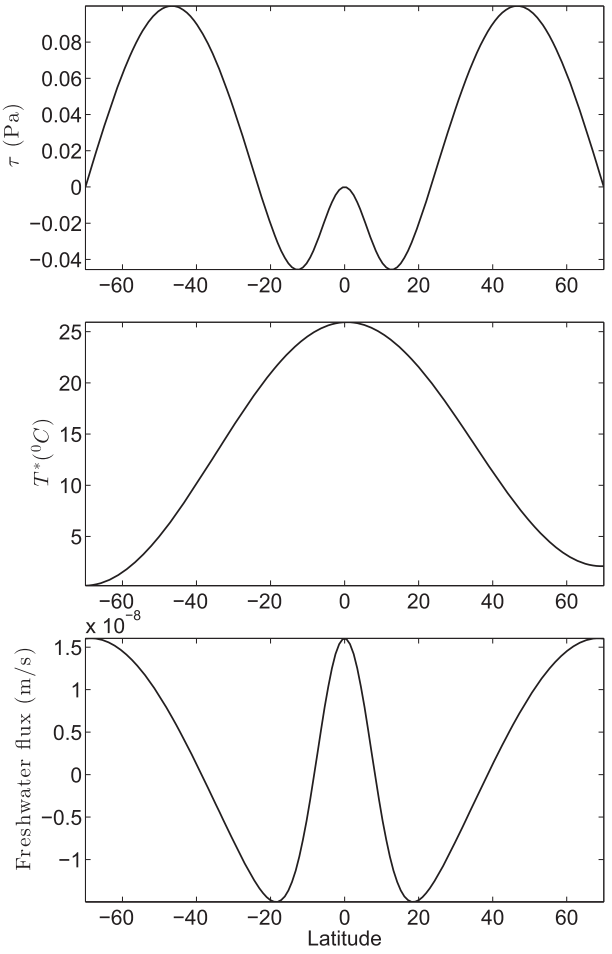

FIG. 6. Forcing fields as a function of latitude: (top) wind stress, (middle) relaxation temperature, and (bottom) freshwater flux.

regions of weak stratification using the method of Danabasoglu and McWilliams (1995).

Tracers are advected using the second-order moments (SOM) scheme of Prather (1986) and diffused using a vertical diffusivity κ, which is surface intensified to mimic an idealized mixed layer such that

$$\kappa = \kappa_\nu + \kappa_m[1 + \tanh(z + d)/d], \tag{17}$$

where $\kappa_\nu = 2 \times 10^{-5}\,\mathrm{m^2\,s^{-1}}$, $\kappa_m = 10^{-2}\,\mathrm{m^2\,s^{-1}}$, and $d = 20\,\mathrm{m}$.

The approach is to study the dependence of the overturning circulation on the length of the narrow basin's eastern boundary, the short continent, keeping everything else fixed. The motivation behind this choice is to keep the total transport of the overturning fixed and in particular the Ekman transport and pumping in the circumpolar region. Specifically, the latitude at which the Ekman pumping changes sign in the model's Southern Ocean is fixed at $\theta_o = -43°$. Thus, the methodology here is complementary to that of Sijp and England (2009) and similar to the approach of Nilsson et al. (2013), but in the context of an ocean-only model.

Residual overturning streamfunction

As a measure of the overturning circulation, we use the zonally integrated residual overturning streamfunction (cf. Wolfe and Cessi 2015), defined as

$$\psi(y, \tilde{b}) \equiv \frac{1}{T}\int_0^T \int_0^{L_x} \int_{-H}^{0} v^\dagger \mathcal{H}[b(x, y, z, t) - \tilde{b}]\, dz\, dx\, dt, \tag{18}$$

where $T = 100\,\mathrm{yr}$, $v^\dagger = v + v_{\mathrm{GM}}$ is the total meridional velocity (the sum of the resolved velocity v and the eddy velocity from the GM parameterization v_{GM}), and $\mathcal{H}$ is the Heaviside step function. The streamfunction ψ is the zonally integrated transport of water above the isopycnal $b(x, y, z, t) = \tilde{b}$. The "vertical" coordinate $\tilde{b}$ is buoyancy; the tilde distinguishes the label of a buoyancy surface from the buoyancy field (Young 2012).

For presentation purposes, ψ is remapped into height coordinates using the mean isopycnal height

$$\zeta(y, \tilde{b}) \equiv -\frac{1}{T}\int_0^T \frac{1}{L_x}\int_0^{L_x} \int_{-H}^{0} \mathcal{H}[b(x, y, z, t) - \tilde{b}]\, dz\, dx\, dt. \tag{19}$$

In height coordinates, ψ advects a modified buoyancy $b^\sharp(y, z)$ that satisfies $\zeta[y, b^\sharp(y, z)] = z$; that is, ψ is constant on $b^\sharp$ contours for purely adiabatic flow.

Because of zonal buoyancy gradients, the remapping distorts the vertical extent of the mixed layer. Buoyancies higher than $40 \times 10^{-3}\,\mathrm{m^2\,s^{-1}}$ are not plotted because the contours are too close together.

4. Short continent at $\theta_s = -45°$, $-35°$, and $-21°$

Provided that the short continent is to the east of the narrow basin, sinking occurs at the northern end of the narrow basin; this result is insensitive to θ_s. The resulting overturning circulations are shown in Fig. 7 (colors), together with $b^\sharp$ (black contours). The cross-equatorial ROC ψ_N^a, zonally integrated over both basins, is approximately 11, 12, and 13 Sv ($1\,\mathrm{Sv} \equiv 10^6\,\mathrm{m^3\,s^{-1}}$) for $\theta_s = -35°, -21°, -45°$, respectively (cf. Fig. 14), rather below the value predicted by the idealized model of section 2. The interhemispheric circulation in the narrow basin is quasi adiabatic: the northward flow at intermediate depths follows isopycnals fairly well in the Southern Hemisphere, while the quasi-adiabatic residual flow in the Northern Hemisphere is augmented

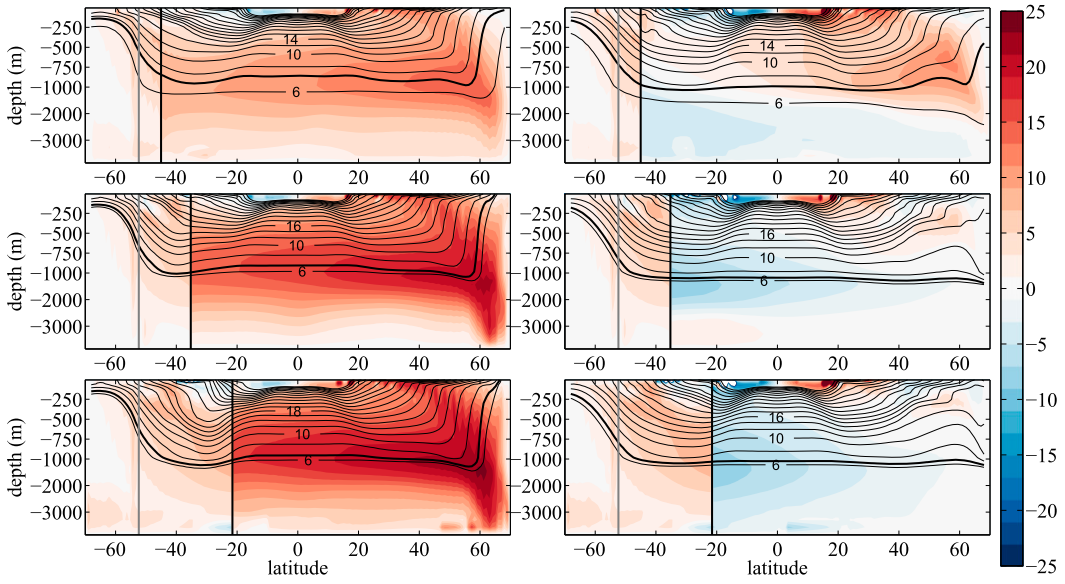

FIG. 7. Residual overturning streamfunction in Sverdrups (color contours; interval 2 Sv) and $b^\sharp \times 10^3$ m s^{-2}, the buoyancy of the surface whose average depth is z (black contours) in the (left) narrow basin and the (right) wide basin for θ_s = (top) −43°, (middle) −35°, and (bottom) −21°. The thick black contour denotes the isopycnal that bounds the upper branch of the ROC: $b_m = 0.0071$ m s^{-2} for $\theta_s = -45°$, $b_m = 0.0066$ m s^{-2} for $\theta_s = 35°$S and −21°. The vertical black line denotes the latitude of the short continent, and the vertical gray line is the latitude of the long continent. South of the short continent the zonal integral of the ROC is over the whole width of the domain.

by a diffusively driven positive cell. There is a weak ROC in the wide basin that decreases as θ_s moves equatorward: it is 3, −5, −6 Sv for $\theta_s = -45°, -35°, -21°$, respectively. This decrease leads to an increase in the transequatorial ROC in the narrow basin, with the sum over both basins remaining almost constant (cf. Fig. 14). This finding is consistent with the results of Sijp and England (2009), who identified the position of the zero Ekman pumping in the Southern Ocean as an important determinant of the AMOC. Here, the wind stress is fixed, but the relative distance of the maximum of $-\tau/f$ to the latitude of the short continent varies, so the two approaches are comparable. In both Sijp and England (2009) and our sets of numerical experiments there is a portion of sinking that shifts between the narrow and wide basins, associated with a change in the interbasin residual transport (see Fig. 10), as the distance $\theta_s - \theta_o$ is varied. The existence of partial sinking in the wide basin is the major point of discrepancy with the conceptual model of section 2, which assumes that all the sinking occurs in one basin. We discuss this point further in the next section.

In addition to the thickness-weighted average transport as a function of latitude and depth, we consider properties integrated above a buoyancy surface b_m selected to approximately divide the upper and lower branches of the overturning. In practice b_m is chosen to go through the maximum of the zonally averaged ROC: this criterion captures most of the transport of the intermediate water cell. The zonally averaged position of this surface is shown by the thick black lines in Fig. 7. We identify the depth of b_m, shown in Fig. 8, as the variable h in the conceptual model of section 2. In all cases the depth of b_m at the eastern boundary of the sinking basin (h_a in section 2) is shallower than that at the eastern boundary of the nonsinking basin (h_p in section 2), as in Jones and Cessi (2016). The minimum difference in the two depths is for $\theta_s = -21°$, as predicted by the conceptual model (cf. with the top panel of Fig. 4). Given that the zero Ekman pumping latitude is $\theta_o = -43°$, the most important difference among the three values of θ_s is that for $\theta_s = -35°$ and −21° the subpolar circumpolar contours are uninterrupted, and there is a single subtropical supergyre in the Southern Hemisphere. For $\theta_s = -45°$, some subpolar circumpolar contours are interrupted by the short continent, and there are two separate subtropical gyres in the Southern Hemisphere. This qualitative change is visualized by the barotropic streamfunction associated with the horizontal velocity integrated from top to bottom shown in Fig. 9, and it leads to a fundamental difference in the interbasin exchange flow.

As a measure of the residual transport exchanged between the two basins we contour in Fig. 10 the pseudostreamfunction associated with the zonal transport above the isopycnal b_m (whose height is given in Fig. 8).

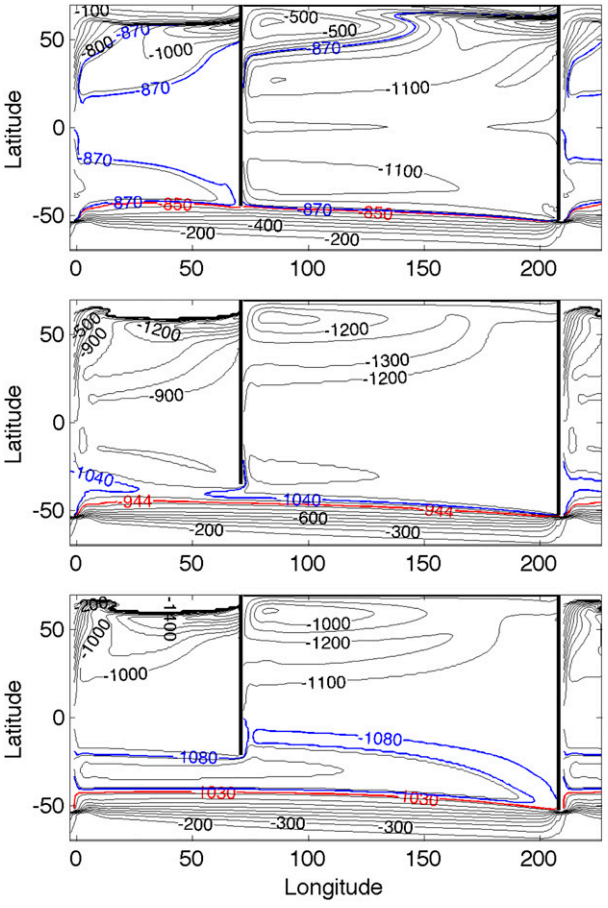

FIG. 8. Contours of the depth (m) of the isopycnal (top) $b_m = 0.0071\,\mathrm{m\,s^{-2}}$ for $\theta_s = -45°$ and of $b_m = 0.0066\,\mathrm{m\,s^{-2}}$ for $\theta_s =$ (middle) $-35°$ and (bottom) $-21°$. The red contour approximately marks the northernmost circumpolar contour, while the blue contour approximately marks the southernmost contour exchanged between the semienclosed basins. The domain is 210°-periodic; the western 20° of the narrow basin is repeated to the right of the figure. Contour interval is 100 m.

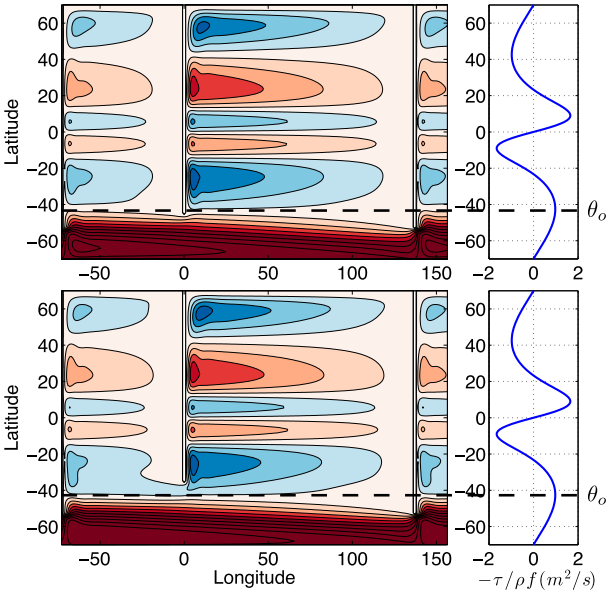

FIG. 9. Barotropic streamfunction (color) associated with the horizontal velocity integrated from top to bottom for $\theta_s =$ (top left) $-45°$ and (bottom left) $-35°$. Notice the transition from a single subtropical supergyre in the Southern Hemisphere when $\theta_s > \theta_o$ in the bottom-left panel to two separate gyres when $\theta_s < \theta_o$ in the top-left panel. The contour interval is 10 Sv, negative values are blue, and positive values are red. The horizontal dashed lines marks the latitude of zero Ekman pumping $\theta_o = -43°$. (right) $-\tau/(\rho f)$ $(\mathrm{m^2\,s^{-1}})$ as a function of latitude. The domain is 210°-periodic; the western 20° of the narrow basin is repeated to the right of the figure in the left panels.

The pseudostreamfunction ϕ is constructed by adding the diapycnal contribution to the integrated zonal transport, that is,

$$\phi = -\frac{1}{T}\int_0^T dt \int_{-L}^{y} d\hat{y}\left\{\int_{-H}^{0} u^{\dagger}(x,\hat{y},z)\mathcal{H}[b(x,\hat{y},z,t) - b_m]\,dz - \int_0^x d\hat{x}\varpi(\hat{x},\hat{y})\right\}, \tag{20}$$

where $u^{\dagger}$ is the sum of the resolved plus parameterized eddy zonal velocities, and ϖ is the diapycnal velocity across the same isopycnal. This construction gives some apparent flow through the solid boundaries, but it has the advantage of illustrating the contribution of all the components of the ROC above the isopycnal b_m, including that due to diapycnal mixing. This view emphasizes the different horizontal paths of the exchange flow, highlighted by thick contours in Fig. 10.

For $\theta_s = -45°$, the exchange flow exits the passive basin on the western boundary, immediately turns east in a narrow zonal jet flowing eastward along the circumpolar region, and enters the active basin on the western boundary along the long continent; this is the classic cold-route pattern. From there, the wind-driven gyres induce large-scale meanders, modulating the meridional transport into alternating broad flows around the anticlockwise gyres and narrow western boundary currents to the west of clockwise gyres. Finally, the exchange flow sinks in the northeast sector of the active basin. For $\theta_s = -35°$ and $-21°$, the exchange flow occurs from the western boundary of the passive basin directly onto the eastern boundary of the active basin along the short continent via a westward flow; this is the classic warm-route pattern.

A complementary view of the residual flow is given by particle displacements, using the 3D Eulerian plus parameterized eddy velocity to advect Lagrangian parcels. We seed 1000 particles in the top grid level along the latitude of maximum northward Ekman transport in the

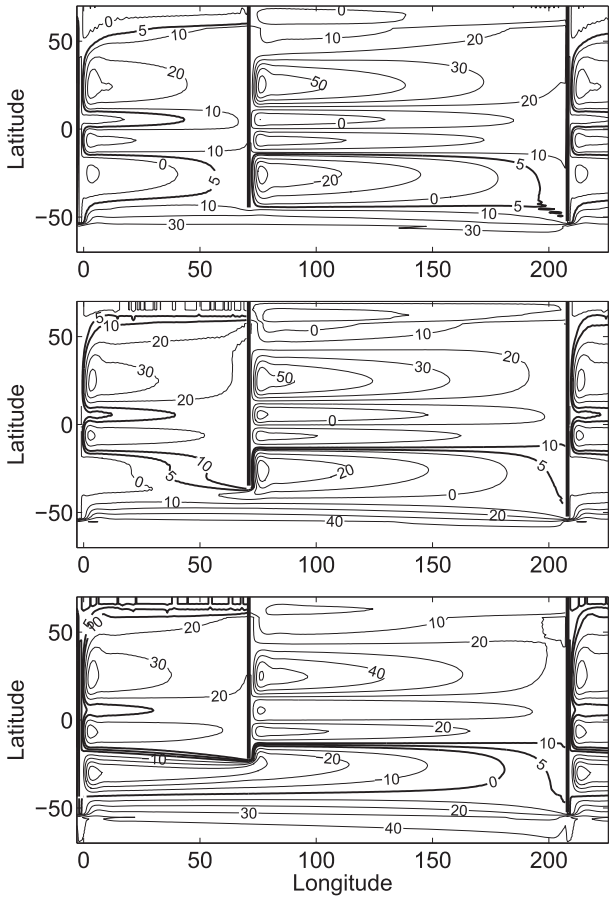

FIG. 10. Pseudostreamlines of the transport (Sv) (top) above $b_m = 0.0071\,\mathrm{m\,s^{-2}}$ for $\theta_s = -45°$, and above $b_m = 0.0066\,\mathrm{m\,s^{-2}}$ for θ_s = (middle) −35° and (bottom) −21°. The pseudostreamlines are constructed by integrating in latitude the sum of the thickness-weighted zonal flow plus the diapycnal velocity. The contour interval is 10 Sv for the thin lines and 5 Sv for the thick lines, which highlight the interbasin exchange flow. The domain is 210° − periodic; the western 20° of the narrow basin is repeated to the right of the figure.

passive basin sector of the Southern Hemisphere and mark their position every 14 days. Two representative particle paths are shown in Fig. 11: one for $\theta_s = -45°$ (top panel) and one for $\theta_s = -35°$ (bottom panel). In both cases the particles move northward near the surface, then downward and around the subtropical gyre of the Southern Ocean. For $\theta_s = -45°$ (Fig. 11, top panel), the particle is then entrained into the cyclonic circulation south of the subtropical gyre and carried circumpolarly around the long continent into the sinking basin, where it is eventually drained out of the upper branch of the ROC. For $\theta_s = -35°$ (Fig. 11, bottom panel), the particle exits the passive basin around the short continent, moving westward into the sinking basin even in the region of eastward Sverdrup flow. We have verified that of the 1000 particles initialized along θ_o, none takes the warm route for $\theta_s = -45°$, and none takes the cold route for $\theta_s = -35°, -21°$.

As for the amplitude of the exchange flow, the prediction of the conceptual model (6) has a weak dependence of ψ_U on θ_s, while the 3D computations give $\psi_U = -6.8, -13.3, -14.9$ Sv for $\theta_s = -45°, -35°, -21°$, respectively,[3] that is, an increase in the interbasin exchange as the short continent moves equatorward. Comparing with Fig. 7, we attribute this discrepancy to the presence of partial sinking in the wide basin, a process not contemplated by the conceptual model.

Exchanging the widths of the basin

In the configurations examined so far, sinking always occurs in the narrow basin, which also has the short continent at its eastern side. Because sinking in the narrow basin is favored even for equal continent lengths (Jones and Cessi 2016), it is not clear whether the width of the basin or the warm-route exchange flow is the dominant process determining the sinking location. This question motivates the experiment analyzed in this subsection, where the widths of the basins are exchanged, thus placing the short continent on the eastern side of the wide basin. We chose the southern latitude of the short continent to be −21°, that is, the most equatorward among those discussed previously. Figure 12 shows the ROC for this experiment, and it is clear that the overturning is now sinking in the wide basin. Analysis of the height and interbasin transport (Fig. 13) shows that the exchange between the two basins occurs through the warm route. However, because the exchange is from the narrow to the wide basin, the interbasin westward flow is smaller than in the configuration examined in the previous subsection: $\psi_U = -6.5$ Sv instead of -13.5 Sv, about a factor of 2 smaller, as predicted by the conceptual model [cf. (10)].

When the interbasin flow is small, the salt exchange is also reduced, as we will see in the next section. Nevertheless, with the short continent on the eastern boundary of the wide basin, the preference for narrow basin sinking is suppressed. Nilsson et al. (2013) found in a coupled ocean–atmosphere model that the narrow basin preference dominates over the short-continent preference. In our case, the additional feedback of more precipitation in the wide basin is absent, and for zonally symmetric freshwater flux, the warm-route salt

[3] The interbasin zonal exchange is estimated by taking the difference of the zonal transports along the two sections south of the continents, and the sign of the value for $\theta_s = -45°$ is reversed as in the conceptual model.

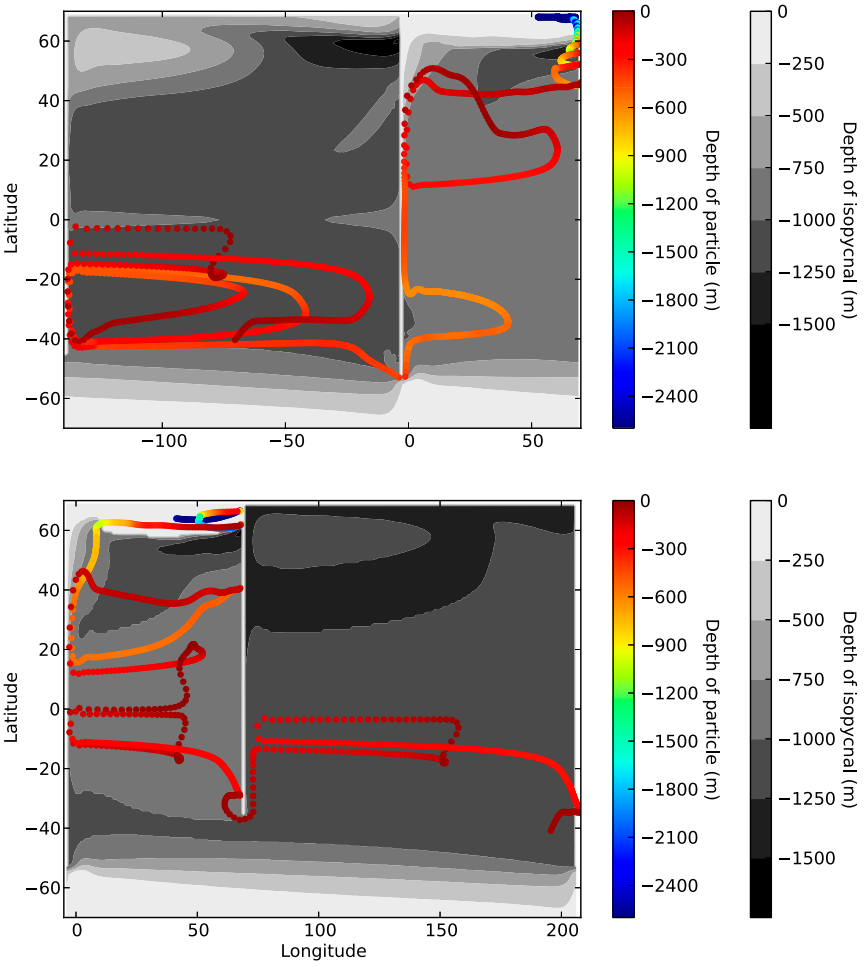

FIG. 11. The depth (m, grayscale) of the isopycnals (top) $b_m = 0.0071\,\mathrm{m\,s^{-2}}$ for $\theta_s = -45°$ and (bottom) of $b_m = 0.0066\,\mathrm{m\,s^{-2}}$ for $\theta_s = -35°$. The position of a particle advected by the residual velocity is shown in rainbow colors, with one point plotted every 14 days, and the color indicates particle depth (m). The active basin is plotted to the right in the top panel and to the left in the bottom panel, so that a continuous particle track is visible in both cases. The particles are initialized at the surface, in the passive sector, at the latitude of maximum Ekman transport $\theta_o = -43°$. The domain is 210°-periodic.

feedback prevails over the narrow basin sinking preference, leading to wide basin sinking, at least for $\theta_s = -21°$.

In summary, the conceptual model of section 2 predicts that the total ROC transport and the interbasin exchange is approximately independent of θ_s, as long as the short continent is equatorward of the zero Ekman pumping line (cf. Fig. 4, bottom panel). In the primitive equation calculations, we find a small dependence on geometry of the transequatorial residual transport (cf. Fig. 14). Given the uncertainty in choosing which isopycnal best marks the bottom of the upper branch of the ROC, we believe that the small differences among the transports are not significant. Nevertheless, we note that none of the configurations reaches the theoretical limit of 17.5 Sv of total sinking dictated by the zonally integrated Ekman transport in the circumpolar region plus the diapycnal upwelling.

5. Salinification through the warm-route exchange

Because of the rapid relaxation to a prescribed surface temperature, the dynamical component of the surface buoyancy is primarily determined by salinity. As a simple diagnostic of the freshwater content in the upper branch of the ROC, we plot in Fig. 15 the salinity vertically and zonally averaged above the isopycnal b_m. The salinity distribution for $\theta_s = -45°$ (top left of Fig. 15) is qualitatively the same as in the case examined by Jones and Cessi (2016) with equal continent lengths; the salinity is higher in the wider basin, except in the subpolar

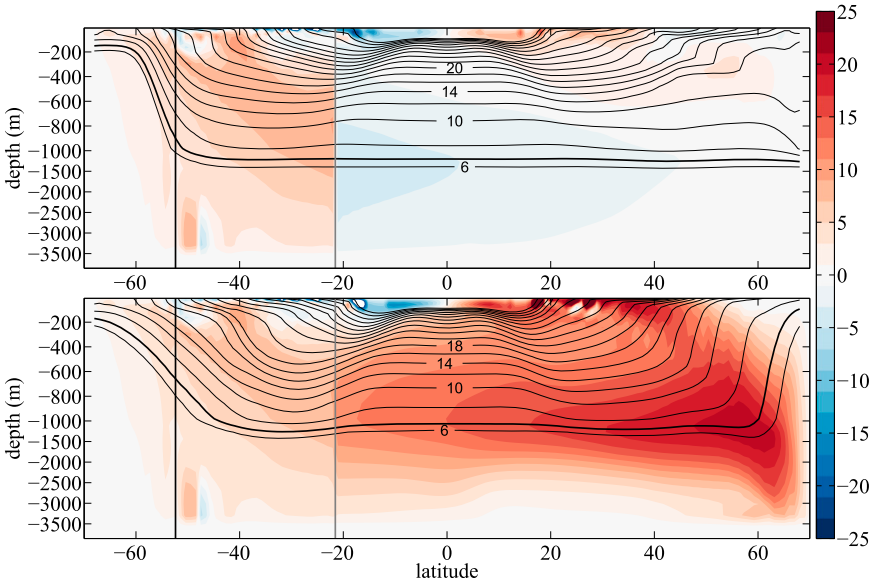

FIG. 12. Residual overturning streamfunction (Sv, color contours, interval 2 Sv) and $b^\sharp \times 10^3\,\mathrm{m\,s^{-2}}$, the buoyancy of the surface whose average depth is z (black contours) in the (top) narrow basin and the (bottom) wide basin, for $\theta_s = -21°$, and the basin widths exchanged relative to the configuration shown in Fig. 7. The thick black contour denotes the isopycnal that bounds the upper branch of the ROC, given by $b_m = 0.0066\,\mathrm{m\,s^{-2}}$. The vertical black line denotes the latitude of the long continent, and the vertical gray line is the latitude of the short continent. South of the short continent the zonal integral for the ROC is over the whole width of the domain in both panels.

region of the Northern Hemisphere where sinking occurs because of the salt advection feedback by the ROC. However, this process produces only a small increase of the salinity in the active over the passive basin. Thus, there is a small amount of sinking in the Northern Hemisphere of the wide basin, which extends across the equator (top-right panel of Fig. 7).

When $|\theta_s| < |\theta_o|$, that is, for $\theta_s = -35°, -21°$, the warm-route exchange advects very effectively high-salinity water in the subtropical region from the passive to the active basin, so that the salinity is higher in the active basin everywhere north of θ_s. Although the exchange flow increases substantially as θ_s moves equatorward, the interbasin salinity differences are about the same in the two cases. The only small difference is that, in the subpolar regions, the wide basin is slightly fresher in the Northern Hemisphere and slightly saltier in the Southern Hemisphere for $\theta_s = -21°$ relative to the case with $\theta_s = -35°$, leading to a larger negative cell in the Southern Hemisphere (cf. the middle and bottom panels of Fig. 7). Because the total ROC transport is fixed by the circumpolar wind stress, this leads to a slightly larger overturning in the narrow basin for $\theta_s = -21°$, in agreement with the findings of Sijp and England (2009).

In the case where the basin widths are exchanged (bottom right of Fig. 15), sinking occurs in the wide basin, and the warm-route inflow from the narrow to the wide basin is smaller than for narrow basin sinking. This leads to a smaller salinity difference in the high latitudes of the Northern Hemisphere compared to the narrow basin sinking (cf. the left and right bottom panels of Fig. 15).

Comparing the salinity differences between the active and passive basins in the cold-route exchange regime (Fig. 15, top-left panel) with those in the warm-route regime (Fig. 15, top-right and bottom panels), we conclude that the warm-route exchange is very effective at salinifying the receiving basins, and in this sense the shortness of the eastern boundary is a more important ocean-only process favoring Atlantic sinking than the narrow width of the basin. It is a remarkable coincidence that both geometrical effects are present in the current geographical configuration of the World Ocean, and both lead to a sinking preference in the Atlantic, even without any asymmetry in the atmospheric forcings.

6. Summary and conclusions

We have studied the residual overturning circulation in a simplified configuration of the World Ocean, with one wide and one narrow basin connected by a reentrant channel and with different meridional extents of the

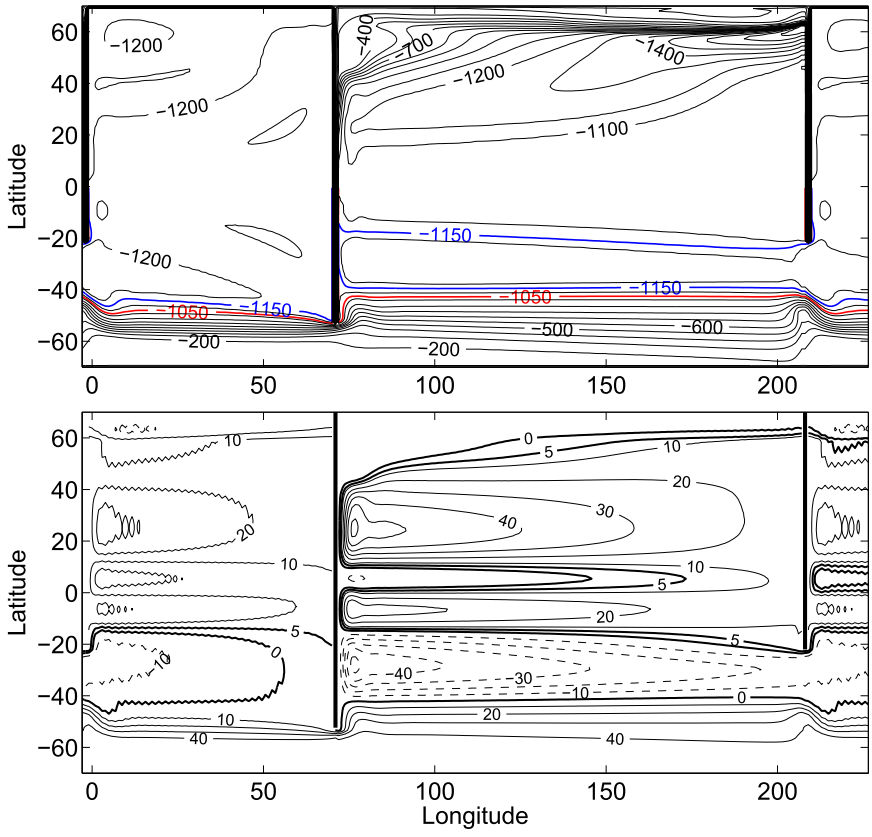

FIG. 13. (top) Contours of the height (m) of the isopycnal $b_m = 0.0066\,\mathrm{m\,s^{-2}}$. Contour interval is 100 m. The red contour approximately marks the northernmost circumpolar contour, while the blue contour approximately marks the southernmost contour connecting the two semienclosed basins. (Bottom) Pseudostreamlines of the transport (Sv) above $b_m = 0.0066\,\mathrm{m\,s^{-2}}$ constructed by integrating in latitude the sum of the thickness-weighted zonal flow plus the diapycnal velocity. The contour interval is 10 Sv for the thin lines and 5 Sv for the thick lines, which highlight the interbasin exchange flow. In both panels, $\theta_s = -21°$, with the narrow and wide basin exchanged; the domain is 210°-periodic, and the western 20° of the narrow basin is repeated to the right of the figure.

continents bounding the basins in the Southern Hemisphere. We show that if the southern edge of the short continent is poleward of the zero Ekman pumping line separating the Southern Ocean subtropical and subpolar gyres, the interbasin exchange associated with the upper branch of the ROC occurs around the tip of the long continent, that is, via the cold route. Otherwise, the interbasin exchange of the upper branch of the ROC is around the tip of the short continent, that is, via the warm route. In the latter case, the ROC transport is approximately given by the maximum Ekman transport in the circumpolar region, and the wind stress that matters is at the zero Ekman pumping latitude.

We note that none of the configurations that we examined exhibits a mixture of the two types of exchange, while some of the GCM diagnostics in the more complex World Ocean configuration attribute a small contribution to the cold route (Speich et al. 2001). This difference might be due to the simplified wind stress forcing (steady, zonally symmetric) and geometry.

A conceptual model of the transport budget shows that, for both routes, if sinking occurs in a single basin, the interbasin transport is approximately given by the portion of Ekman transport in the passive (nonsinking) basin sector, and it is therefore larger when the receiving basin is the narrower one. The net result is that the meridional overturning circulation prefers a state with sinking at the northern edge of the basin with the short continent to the east and even more so if the basin is narrow, just as is the case for the Atlantic Ocean.

As discussed in Jones and Cessi (2016), the salt advection feedback is more effective in a narrow basin than in a wide basin, even when the continent lengths are equal. For the cases examined in Jones and Cessi (2016),

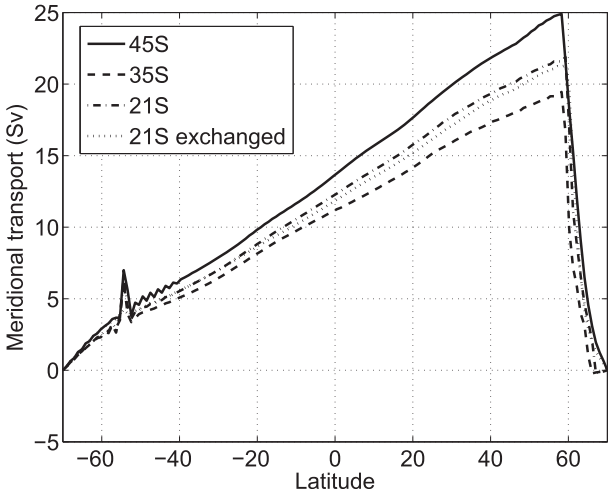

FIG. 14. Meridional residual transports vertically integrated above b_m and zonally integrated across the whole width of the domain as a function of latitude.

the southern limit of the meridional continents is poleward of the zero Ekman pumping line, and the interbasin exchange occurs via the cold route, which is not a very effective way of transferring salt from the passive to the active basin. Having a short continent on the eastern boundary terminating equatorward of the zero Ekman pumping line enables a direct route for subtropical salt export from the passive to the active basin (the warm route). This process salinifies the active basin very effectively.

We find that the warm-route westward flow can take place regardless of whether the southern edge of the short continent is in the region of eastward or westward Sverdrup flow of the supergyre. According to the conceptual model, this interbasin flow is not in Sverdrup balance, but it is the subsurface return of the Ekman transport, so its dynamics depend on the details of the model's formulation (Pedlosky 1987; Parsons 1969). In the conceptual model of section 2, this return flow is assumed to occur uniformly in the depth range of the MOC upper branch, but it is not clear how it is vertically distributed in the primitive equation model.

In our numerical computations the warm-route interbasin residual exchange increases substantially as the termination latitude of the short continent decreases; this increase is accompanied by a small salinity difference between the active and passive basins and between the salinity in the subpolar Northern and Southern

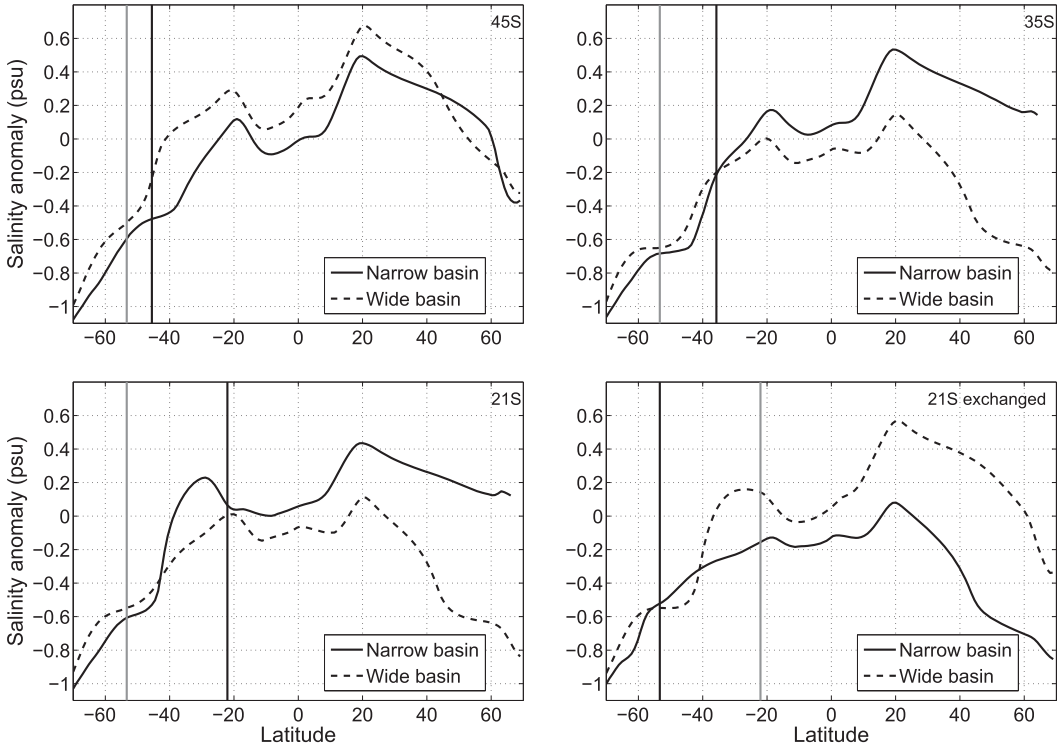

FIG. 15. Salinity anomaly, relative to 35 psu, zonally and vertically averaged above b_m as a function of latitude, for θ_s = (top left) −45°, (top right) −35°, (bottom left) −21°, and (bottom right) −21° with basin widths exchanged. The black vertical line shows the termination latitude of the continent east of the narrow basin, while the gray vertical line shows the termination latitude of the continent west of the narrow basin.

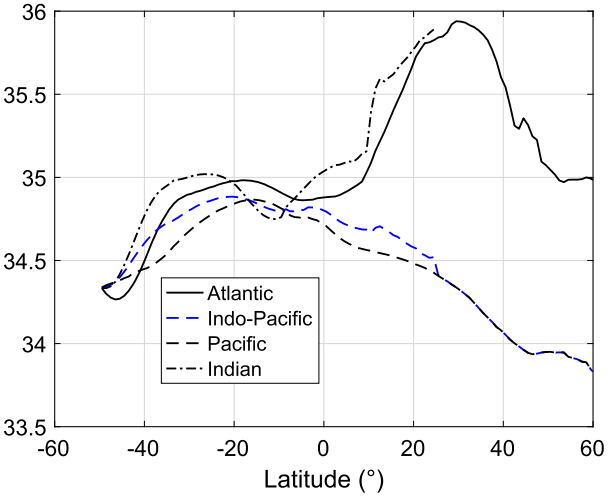

FIG. 16. *World Ocean Atlas* salinity averaged in time over the period 1955–2012, in longitude over each basin and in depth over the top 1000 m.

Hemisphere regions. The salinity distribution can allow a small range of isopycnals to be shared between the Southern Ocean and the Northern Hemisphere of the passive basin, allowing some sinking in the passive basin (de Boer et al. 2008). In turn, this cell can weaken the overturning in the active basin, given that the total overturning is fixed by the upwelling sources (the wind-driven upwelling in the circumpolar Southern Ocean and the diapycnal mixing). This important feedback is not included in the conceptual model, which assumes a priori that sinking only occurs in the active basin. A more sophisticated conceptual model would have to quantify the range of surface isopycnals shared between the circumpolar region and the Northern Hemisphere in both basins and relate the surface buoyancy to the transport of temperature and salinity by the ROC.

Our work demonstrates that the asymmetry in the geometry of the oceans, that is, a continent terminating equatorward of the zero Ekman pumping line on the eastern side of the narrow basin, is sufficient to create a substantial asymmetry in the upper-ocean salinity distribution even in the absence of zonal asymmetries in the surface freshwater flux, wind stress, and temperature distributions. As shown in Fig. 15, for $\theta_s = -35°$ the upper-ocean average salinity in the subpolar gyre of the narrow basin to the west of the short continent is 1 psu higher than in the corresponding region of the wide basin. This contrast, essential for the location of the sinking branch of the MOC, is comparable to the observed, annual, average difference between the subpolar North Atlantic and subpolar North Pacific, shown in Fig. 16 (Levitus et al. 2013). On the other hand, the difference in the averaged upper-ocean salinity generated in the subtropical region by the symmetrically forced model is substantially smaller than the observed one; in this region the asymmetry in the surface freshwater flux must be important.

Acknowledgments. CSJ and PC are supported by the National Science Foundation under Grants OCE-1258887 and OCE-1634128. Computational resources were provided by XSEDE consortium, which is supported by National Science Foundation Grant ACI-1053575. Alexandre Diet is gratefully acknowledged for providing preliminary solutions of the conceptual model. PC is grateful to Donata Giglio for help with the *World Ocean Atlas*. CSJ is grateful to Jinbo Wang, who contributed the particle trajectory code.

REFERENCES

Allison, L. C., 2009: Spin-up and adjustment of the Antarctic Circumpolar Current and global pycnocline. Ph.D. thesis, University of Reading, 207 pp.

Broecker, W. S., 1991: The great ocean conveyor. *Oceanography*, **4**, 79–89, doi:10.5670/oceanog.1991.07.

Danabasoglu, G., and J. C. McWilliams, 1995: Sensitivity of the global ocean circulation to parameterizations of mesoscale tracer transports. *J. Climate*, **8**, 2967–2987, doi:10.1175/1520-0442(1995)008<2967:SOTGOC>2.0.CO;2.

de Boer, A. M., J. Toggweiler, and D. Sigman, 2008: Atlantic dominance of the meridional overturning circulation. *J. Phys. Oceanogr.*, **38**, 435–450, doi:10.1175/2007JPO3731.1.

Durgadoo, J. V., B. R. Loveday, C. J. Reason, P. Penven, and A. Biastoch, 2013: Agulhas leakage predominantly responds to the Southern Hemisphere westerlies. *J. Phys. Oceanogr.*, **43**, 2113–2131, doi:10.1175/JPO-D-13-047.1.

Ferrari, R., S. M. Griffies, A. J. G. Nurser, and G. K. Vallis, 2010: A boundary-value problem for the parameterized mesoscale eddy transport. *Ocean Modell.*, **32**, 143–156, doi:10.1016/j.ocemod.2010.01.004.

Ferreira, D., J. Marshall, and J.-M. Campin, 2010: Localization of deep water formation: Role of atmospheric moisture transport and geometrical constraints on ocean circulation. *J. Climate*, **23**, 1456–1476, doi:10.1175/2009JCLI3197.1.

Gent, P., and J. C. McWilliams, 1990: Isopycnal mixing in ocean circulation models. *J. Phys. Oceanogr.*, **20**, 150–155, doi:10.1175/1520-0485(1990)020<0150:IMIOCM>2.0.CO;2.

Gill, A. E., 1968: A linear model of the Antarctic Circumpolar Current. *J. Fluid Mech.*, **32**, 465–488, doi:10.1017/S0022112068000868.

Gnanadesikan, A., 1999: A simple predictive model for the structure of the oceanic pycnocline. *Science*, **283**, 2077–2079, doi:10.1126/science.283.5410.2077.

Gordon, A. L., 1986: Interocean exchange of thermocline water. *J. Geophys. Res.*, **91**, 5037–5046, doi:10.1029/JC091iC04p05037.

——, R. F. Weiss, W. M. Smethie, and M. J. Warner, 1992: Thermocline and intermediate water communication between the South Atlantic and Indian Oceans. *J. Geophys. Res.*, **97**, 7223–7240, doi:10.1029/92JC00485.

Hughes, T. M. C., and A. J. Weaver, 1994: Multiple equilibria of an asymmetric two-basin ocean model. *J. Phys. Oceanogr.*, **24**, 619–637, doi:10.1175/1520-0485(1994)024<0619:MEOAAT>2.0.CO;2.

Jones, C. S., and P. Cessi, 2016: Interbasin transport of the meridional overturning circulation. *J. Phys. Oceanogr.*, **46**, 1157–1169, doi:10.1175/JPO-D-15-0197.1.

Levitus, S., and Coauthors, 2013: The World Ocean database. *Data Sci. J.*, **12**, WDS229–WDS234, doi:10.2481/dsj.WDS-041.

Marshall, D. P., R. D. Munday, L. C. Allison, R. J. Hay, and H. L. Johnson, 2016: Gill's model of the Antarctic Circumpolar Current, revisited: The role of latitudinal variations in wind stress. *Ocean Modell.*, **97**, 37–51, doi:10.1016/j.ocemod.2015.11.010.

Marshall, J., A. Adcroft, C. Hill, L. Perelman, and C. Heisey, 1997a: A finite-volume, incompressible Navier Stokes model for studies of the ocean on parallel computers. *J. Geophys. Res.*, **102**, 5753–5766, doi:10.1029/96JC02775.

——, C. Hill, L. Perelman, and A. Adcroft, 1997b: Hydrostatic, quasi-hydrostatic, and nonhydrostatic ocean modeling. *J. Geophys. Res.*, **102**, 5733–5752, doi:10.1029/96JC02776.

Munk, W. H., 1966: Abyssal recipes. *Deep-Sea Res. Oceanogr. Abstr.*, **13**, 707–730, doi:10.1016/0011-7471(66)90602-4.

Nikurashin, M., and R. Ferrari, 2013: Overturning circulation driven by breaking internal waves in the deep ocean. *Geophys. Res. Lett.*, **40**, 3133–3137, doi:10.1002/grl.50542.

Nilsson, J., P. L. Langen, D. Ferreira, and J. Marshall, 2013: Ocean basin geometry and the salinification of the Atlantic Ocean. *J. Climate*, **26**, 6163–6184, doi:10.1175/JCLI-D-12-00358.1.

Okazaki, Y., A. Timmermann, L. Menviel, N. Harada, A. Abe-Ouchi, M. Chikamoto, A. Mouchet, and H. Asahi, 2010: Deepwater formation in the North Pacific during the last glacial termination. *Science*, **329**, 200–204, doi:10.1126/science.1190612.

Parsons, A. T., 1969: A two-layer model of Gulf Stream separation. *J. Fluid Mech.*, **39**, 511–528, doi:10.1017/S0022112069002308.

Pedlosky, J., 1987: On Parsons' model of the ocean circulation. *J. Phys. Oceanogr.*, **17**, 1571–1582, doi:10.1175/1520-0485(1987)017<1571:OPMOTO>2.0.CO;2.

Prather, M. J., 1986: Numerical advection by conservation of second-order moments. *J. Geophys. Res.*, **91**, 6671–6681, doi:10.1029/JD091iD06p06671.

Reid, J. L., Jr., 1961: On the temperature, salinity, and density differences between the Atlantic and Pacific Oceans in the upper kilometre. *Deep-Sea Res.*, **7**, 265–275, doi:10.1016/0146-6313(61)90044-2.

Redi, M. H., 1982: Oceanic isopycnal mixing by coordinate rotation. *J. Phys. Oceanogr.*, **12**, 1154–1158, doi:10.1175/1520-0485(1982)012<1154:OIMBCR>2.0.CO;2.

Rintoul, S. R., 1991: South Atlantic interbasin exchange. *J. Geophys. Res.*, **96**, 2675–2692, doi:10.1029/90JC02422.

Sijp, W. P., and M. H. England, 2009: Southern Hemisphere westerly wind control over the ocean's thermohaline circulation. *J. Climate*, **22**, 1277–1286, doi:10.1175/2008JCLI2310.1.

Speich, S., B. Blanke, and G. Madec, 2001: Warm and cold water routes of an OGCM thermohaline conveyor belt. *Geophys. Res. Lett.*, **28**, 311–314, doi:10.1029/2000GL011748.

St. Laurent, L. C., H. L. Simmons, and S. R. Jayne, 2002: Estimating tidally driven mixing in the deep ocean. *Geophys. Res. Lett.*, **29**, 2106, doi:10.1029/2002GL015633.

Stommel, H., 1961: Thermohaline convection with two stable regimes of flow. *Tellus*, **13**, 224–230, doi:10.3402/tellusa.v13i2.9491.

Toggweiler, J. R., and B. Samuels, 1993: Is the magnitude of the deep outflow from the Atlantic Ocean actually governed by Southern Hemisphere winds? *The Global Carbon Cycle*, M. Heimann, Ed., NATO ASI Series, Vol. 15, Springer, 333–366, doi:10.1007/978-3-642-84608-3_13.

Warren, B. A., 1983: Why is no deep water formed in the North Pacific? *J. Mar. Res.*, **41**, 327–347, doi:10.1357/002224083788520207.

Weaver, A. J., C. M. Bitz, A. F. Fanning, and M. M. Holland, 1999: Thermohaline circulation: High-latitude phenomena and the difference between the Pacific and Atlantic. *Annu. Rev. Earth Planet. Sci.*, **27**, 231–285, doi:10.1146/annurev.earth.27.1.231.

Wolfe, C. L., and P. Cessi, 2015: Multiple regimes and low-frequency variability in the quasi-adiabatic overturning circulation. *J. Phys. Oceanogr.*, **45**, 1690–1708, doi:10.1175/JPO-D-14-0095.1.

Young, W. R., 2012: An exact thickness-weighted average formulation of the Boussinesq equations. *J. Phys. Oceanogr.*, **42**, 692–707, doi:10.1175/JPO-D-11-0102.1.

Zhang, R., and T. L. Delworth, 2005: Simulated tropical response to a substantial weakening of the Atlantic thermohaline circulation. *J. Climate*, **18**, 1853–1860, doi:10.1175/JCLI3460.1.